INTERNATIONAL JOURNAL FOR NUMERICAL METHODS IN FLUIDS
Int. J. Numer. Meth. Fluids 2005; **47**:603–617
Published online in Wiley InterScience (www.interscience.wiley.com). DOI: 10.1002/fld.834

Modelling of inflow boundary conditions for image-based simulation of cerebrovascular flow

Marie Oshima[1,*,†], Hiroyuki Sakai[2] and Ryo Torii[1]

[1]*Institute of Industrial Science, University of Tokyo, Komaba 4-6-1 Meguro-ku, Tokyo 153-8505, Japan*
[2]*Higashi Fuji Research Institute, Toyota Motor Corporation, 1200 Onjuku Susono-shi, Shizuoka-ken, 410-1193, Japan*

SUMMARY

The goals of this study were to model the secondary flow components of inflow boundary conditions and examine the effects of inflow boundary conditions on cerebral haemodynamics. Finite element simulations were conducted for the curved pipe model and the results were compared with PIV measurements. The vortex structures of secondary flow were modelled in terms of the Dean number, which is a function of curvature and the Reynolds number. The modelled secondary flow was superimposed on the axial velocity profile obtained by ultrasound as the inflow boundary condition. The image-based simulation was performed for an aneurysm of the middle cerebral artery using the modelled inflow boundary conditions. Results of inflow models with and without secondary flow are compared and show differences in flow patterns and wall shear stress distributions depending on the inflow model. Copyright © 2005 John Wiley & Sons, Ltd.

KEY WORDS: computational haemodynamics; image-based simulation; boundary conditions; secondary flow; PIV

1. INTRODUCTION

To predict the formation and rupture of cerebral aneurysms, detailed information of haemodynamic quantities, such as distribution and magnitude of wall shear stress or velocity are needed. However, these values are difficult to measure *in vivo* by medical imaging techniques such as MRI or CT due to limited resolution and data acquisition of the available systems. In particular, measurement of haemodynamic quantities of the cerebral circulation is challenging due to its geometric complexity and the presence of the skull and small vessels. *In vivo* image-based simulations have emerged as powerful tools for haemodynamic study [1, 2]. We

*Correspondence to: Marie Oshima, Institute of Industrial Science, University of Tokyo, Komaba 4-6-1 Meguro-ku, Tokyo 153-8505, Japan.
†E-mail: marie@iis.u-tokyo.ac.jp

Received 3 February 2004
Accepted 18 August 2004

have studied medical image-based simulation and database systems to investigate the effects of vascular morphology on cerebral haemodynamics [3, 4].

The *in vivo* image-based model performs detailed three-dimensional simulations for analysis regions whose geometric information, such as vascular morphology, is obtained from medical images. In general, the analysis focuses on a localized region, such as an area near the cerebral aneurysm, because of the need for significant amounts of computer memory and time. Although the analysis region is only a portion of the circulatory system, the simulation has to include the effects from the entire circulatory system. Thus, modelling of proper boundary conditions is essential for the image-based simulation.

This paper focuses on inflow boundary conditions. Velocity is usually prescribed at the inflow boundary as the Dirichlet boundary condition. Mean flow rates can be measured by intracranial ultrasound Doppler or MRI. However measurement locations in the cerebral circulation are limited to the carotid artery or MCA. On the other hand, zero or one-dimensional wave propagation equations are solved numerically to quantify mean flow rate and pressure in the circulatory system [5–7]. Either method provides mean flow rate or the axial component of velocity but cannot prescribe the three-dimensional velocity profile at the inflow boundary. Due to curvature and bifurcation, blood flow through the cerebral circulation produces complex swirl and three-dimensional flow patterns [8]. Thus, inflow boundary conditions require modelling of secondary flow components as well as the axial component.

This paper compares results obtained from both numerical simulations and experiments conducted at the same curvature and Reynolds number ($Re = \rho UL/\mu$, where U is the characteristic velocity, L is the characteristic length, ρ is density, and μ is viscosity) using a curved pipe model, which emulates the curvature of the internal carotid artery (ICA). In addition, the numerical simulations were conducted for the curved pipe model to examine the effects of varying curvatures and Reynolds numbers on the characteristics of secondary flow. The modelling of secondary flow components of the inflow boundary conditions are based on the numerical simulation of the curved pipe model. Finally, the image-based simulations are performed under varying inflow boundary conditions derived from the present model of inflow boundary conditions. The results are compared and discussed to analyse effects of inflow boundary on the haemodynamics of the cerebral arteries and aneurysms.

2. NUMERICAL METHOD

2.1. Governing equations and finite element implementation

Blood flow in the cerebrovascular system is considered incompressible and is governed by the continuity and Navier–Stokes equations, which are written as follows for a computational domain Ω

$$\frac{\partial u_i}{\partial x_i} = 0 \tag{1}$$

$$\rho\left(\frac{\partial u_i}{\partial t} + u_j \frac{\partial u_i}{\partial x_j}\right) = -\frac{\partial P}{\partial x_j}\delta_{ij} + \mu \frac{\partial^2 u_i}{\partial x_j \partial x_j} + f_i \tag{2}$$

where u_i is velocity in the ith direction, ($i = 1$, 2, and 3, which denotes x, y, and z direction, respectively), P is pressure, f_i is body force, and δ_{ij} is the Kronecker delta.

The boundary conditions for Equations (1) and (2) are given by

$$u_i = g_i(x,t) \quad \text{on } \Gamma_g \tag{3}$$

$$t_i = h_i(x,t) \quad \text{on } \Gamma_h \tag{4}$$

$$h_i = \left(-P\delta_{ij} + \mu \frac{\partial u_i}{\partial x_j}\right) n_j \tag{5}$$

where t_i is the ith component of surface traction, n_j is the jth component of a vector normal to the Neumann boundary Γ_h, and Γ_g is the Dirichlet boundary.

The finite element method is used for spatial discretization. The weighted residual method is employed to derive the weak form of Equations (1) and (2). The weak form is derived by integrating the product of the weighting function and the governing equations by parts, then, obtaining an approximation using the Galerkin finite element method, in which the same basic function is used for both the variables and corresponding weighting functions. To satisfy the constraint condition of incompressibility, the mixed finite element method is used such that the order of interpolation for pressure is one order smaller than that for the velocity. Since analyses are conducted in three-dimensions, a brick element with a trilinear function for velocity and a piece-wise constant for pressure are used. The one-point quadrature is applied to the convective terms to avoid numerical instability at a high Reynolds number [4].

Implementation of the finite element equations is performed in a conventional semi-discrete formulation. The numerical algorithm is based on the Marker and Cell (MAC) method, and the second-order Adams–Bashforth method is used for time discretization [2].

2.2. *Womersley solutions for pulsatile flow*

Blood flow is a time-dependent pulsatile flow. If flow rate is known, the analytical solutions for pulsatile flow, which are defined as the Womersley solutions, can be derived. The Womersley solution is a canonical solution of fully developed pulsatile flow in a straight circular cylinder, given by

$$u_z(r,t) = \frac{2B_0}{\pi R^2}\left[1 - \left(\frac{r}{R}\right)^2\right] + \sum_{n=1}^{N} \frac{2B_n}{\pi R^2}\left[\frac{1 - \dfrac{J_0\left(\alpha_n \dfrac{r}{R} i^{3/2}\right)}{J_0(\alpha_n i^{3/2})}}{1 - \dfrac{2J_1(\alpha_n i^{3/2})}{\alpha_n i^{3/2} J_0(\alpha_n i^{3/2})}}\right] e^{inwt} \tag{6}$$

where r is the co-ordinate in the radial direction, R is the radius of the artery, ω is angular velocity of pulsation, J_n is a Bessel function of first order n, $\alpha_n = R\sqrt{n\omega/v}$ is the Womersley parameter of order n, and v is kinematic viscosity. Coefficient B_n is the Fourier coefficient of flow rate, determined by

$$Q(t) \approx \sum_{n=0}^{N} B_n e^{inwt} \tag{7}$$

where $Q(t)$ is the flow rate.

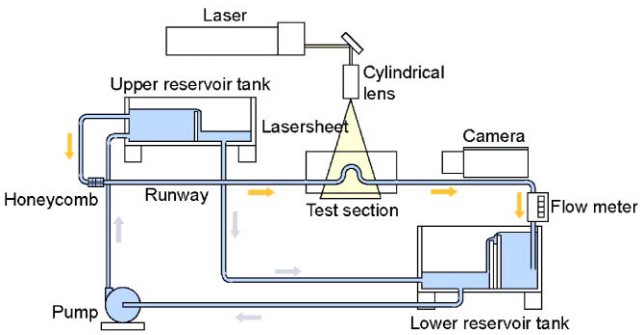

Figure 1. Schematic diagram of PIV measurement system.

3. PIV SYSTEM

PIV is a non-invasive method to measure velocity, which can capture large areas of the flow field with high spatial resolution [9]. In most PIV applications, tracer particle are added to the flow. These particles are illuminated twice within a short time interval. The images of the light scattered by the particles are recorded and the displacement between two particle image frames determines the velocity field.

In general, a PIV system consists of three parts: light source, image recording system, and image processing system. The schematic diagram of the present PIV system is illustrated in Figure 1. The light source consists of a pair of high power double-pulsed Nd:YAG lasers (New Wave Research, Minilase III) with a wavelength of 532 nm and a maximum power of 20 mJ/pulse. The image processing system consists of a CCD camera having a resolution of 1000×1016 pixels (TSI, PIVCAM 10-30). Tracer particles are SiO_2 porous grains with a diameter of 12 mm and specific gravity of 2.1 g/cc. The particles are illuminated in a light sheet 1.0 mm thick; frame rate between two images is 15 fps, which is determined by the repetition rate of the laser.

Images of the particles illuminated by the double-pulsed lasers are recorded by the CCD camera. In the image processing system, each pair of particle images is analysed by a two-frame cross-correlation method to estimate the local displacement of particle image patterns in two proximate times. The interrogation window size is 32×32 pixels on the digital image.

4. CURVED PIPE MODEL

The ICA is a preferential location for aneurysm formation. The ICA contains a complex curvature, which is called the carotid siphon, as shown in Figure 2. Strong secondary flow is generated due to the curvature of the carotid siphon and is carried through the anterior cerebral artery (ACA) and the middle cerebral artery (MCA). In general, inflow boundary conditions are prescribed using the flow rate obtained by ultrasound Doppler or MRI and then applying Equation (6) (Womersley solutions) to obtain the velocity distribution. The Womersley solutions, however, provide only the axial component (z) of pulsatile flow, not the x and y components. The vortex structures depend on curvature and Reynolds number.

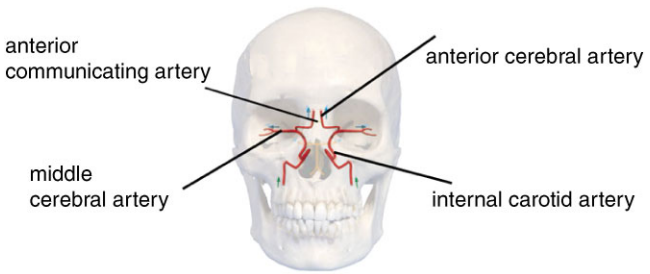

Figure 2. Cerebrovascular network on the anterior side.

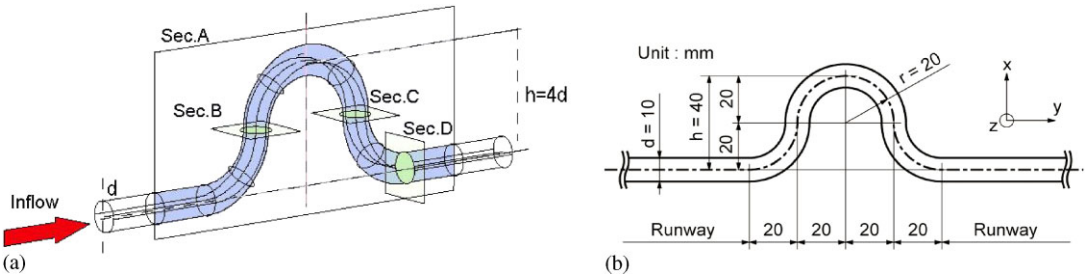

Figure 3. Curved pipe model with measuring sections for comparison between experiment and simulation: (a) schematic illustration of curved pipe model; and (b) curved pipe model for PIV measurement.

If the real geometry is used for the study, it would be difficult to distinguish the effects of curvature and Reynolds number from others due to complex flow features created by complicated geometry. Thus, the inflow boundary conditions were modelled by varying the curvature and Reynolds number using the curved pipe model, which is simple but emulates the curvature of the carotid siphon.

4.1. Numerical and experimental models

Curved pipe models for the simulation and experiments are illustrated in Figures 3(a) and (b), respectively. The diameter of the simulation model is 0.4 cm, which is the average diameter of the ICA. However, the experimental model (constructed of acrylic resin) is scaled 2.5 times larger than the numerical model to obtain a reliable velocity measurement.

The curvature of the curved model is defined by the ratio of height (h) to artery diameter (d). The numerical simulations were conducted for seven different models with curvatures of $h/d = 1.0$, 1.5, 2.0, 2.5, 3.0, 3.5, and 4.0. The practical experiment was conducted for one model of curvature $h/d = 4.0$. Thus, The comparison between the results of the simulation and experiment were performed at a curvature of $h/d = 4.0$.

4.2. Numerical and experimental conditions

For the simulation, velocity in the inflow boundary is given by Equation (6) using the flow rate obtained by ultrasound Doppler. Both the measurement data and the Womersley velocity are depicted in Figure 4. Blood flow in the cerebral artery is assumed to be a Newtonian fluid

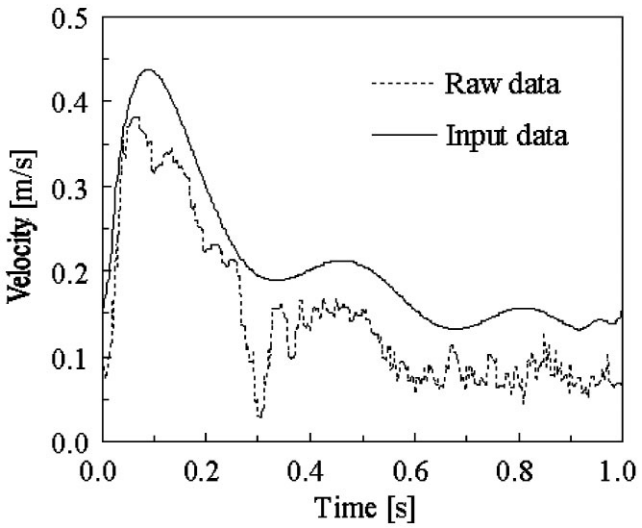

Figure 4. Velocity profiles of the ultrasound Doppler measurement data and the Womersley solutions for pulsatile flow.

and to have a constant kinematic viscosity of 4×10^{-6} m^2/s. The resulting Reynolds number varies from 100 to 450, and the Womersley number is 3.13. The outflow boundary condition for the simulation is a free-stream condition. The boundary condition at the wall is non-slip, and the wall of the artery is assumed to be rigid.

The same outflow boundary and wall boundary conditions were applied to the experimental situation. The fluid used in the experiment was 64% sodium iodide (NaI), which has the same refractive index as acrylic resin, 1.49. The experiment was conducted at the same Reynolds number as that in the simulation by varying the inflow velocity.

4.3. Comparison between numerical results and experimental measurements

The simulation and experimental results are compared for the curved pipe model of curvature $h/d = 4.0$ at Reynolds number 450. The comparison was conducted for velocity fields in sections A (mid-plane parallel to the axis of the model), B, and C (plane perpendicular to the axis of the model) as described in Figure 3(a).

Figures 5(a) and (b) show the velocity vectors and counters of vorticity in section A obtained by PIV measurement and the simulation, respectively. Good agreement existed between the experimental data and numerical results as demonstrated in Figures 5(a) and (b). The velocity vectors and counters of vorticity in section B are depicted in Figures 6(a) and (b) while those in section C are depicted in Figures 7(a) and (b). The curvature generates secondary flow for the numerical simulation and experiment as shown in Figures 6 and 7. One pair of symmetric vortices exists in section B. In contrast, section C contains one pair of large symmetric vortices and another pair of small symmetric vortices. The distributions of velocity vectors and vortices correlate well between the numerical simulation and experiment in each section, which validates the present numerical simulation.

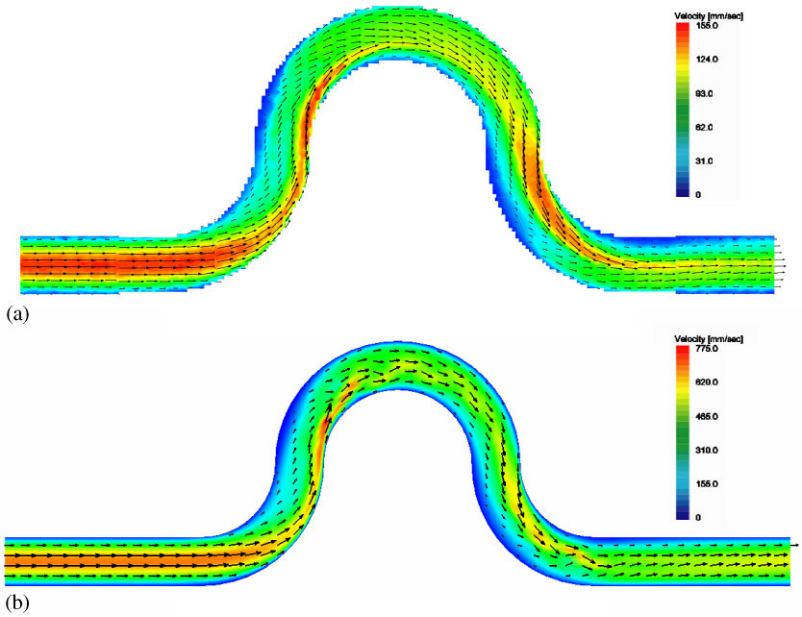

Figure 5. Comparison of velocity fields at section A between PIV experimental data and simulation result at curvature $h = 4d$ and $Re = 450$: (a) velocity field obtained by the PIV measurement; and (b) velocity field obtained by the simulation.

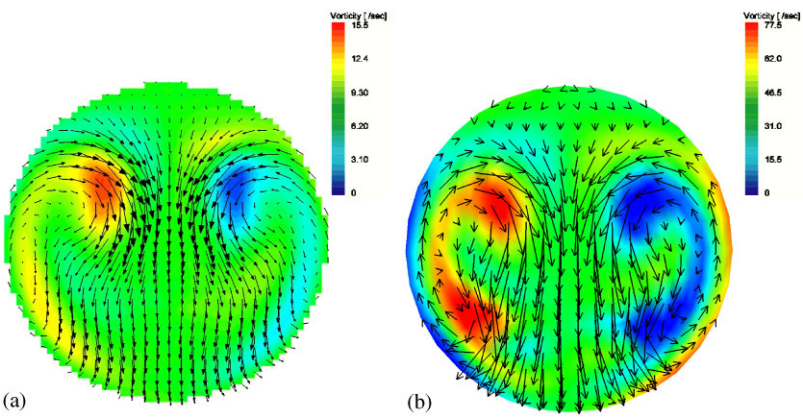

Figure 6. Comparison of velocity fields at section B between PIV experimental data and simulation result at curvature $h = 4d$ and $Re = 450$: (a) velocity field obtained by the PIV measurement; and (b) velocity field obtained by the simulation.

4.4. Vortex structures of secondary flow at steady-state inflow boundary conditions

This study examined the vortex structures with respect to curvature and Reynolds number in the inflow boundary. The curvature was $h/d = 1.0$, 1.5, 2.0, 2.5, 30, 3, and 4.0 with a Reynolds number of $Re = 250$, 350, and 500. Modelling inflow boundary conditions that

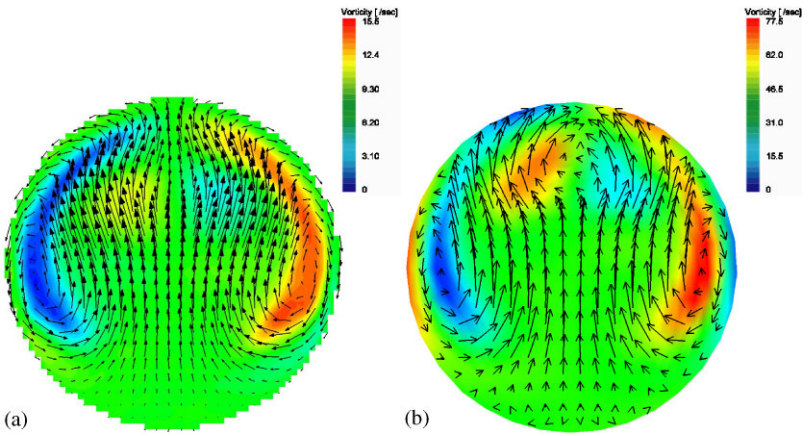

Figure 7. Comparison of velocity fields at section C between PIV experimental data and simulation result at curvature $h = 4d$ and $Re = 450$: (a) velocity field obtained by the PIV measurement; and (b) velocity field obtained by the simulation.

include characteristics of secondary flow with respect to curvature and Reynolds number, depends upon observation of the velocity profiles in the outflow plane, section D, which becomes the inflow boundary for the downstream artery such MCA or ACA.

Figures 8(a)–(c) summarize the velocity and vorticity distributions with respect to curvature and Reynolds number. The vortex structures are categorized as shown in Figures 9(a)–(d). When curvature is small, one pair of outward vortices exists, as shown in Figure 9(b). As Reynolds number increases at small curvature, vorticity increases and the centre of vortex moves downward. As curvature increases, the vortex centre moves upward and a pair of inward vortices begins to appear at the bottom, as shown in Figure 9(b). As curvature continues to increase, two pairs of vortices are formed, as seen in Figure 9(c). When the curvature reaches its highest point, the upper pair of vortices begins to decay and the bottom pair of inward vortices become dominant. The inward vortex moves downward and two pairs of vortices are formed, associated with the increase in curvature.

As shown in Figures 8(a)–(c), certain combinations of curvature and Reynolds number exhibit similar vortex structures. To examine vortex structures associated with changes in curvature and Reynolds number, vortex structures were categorized by Dean number. The Dean number N_D is defined by

$$N_D = R_e\sqrt{\delta} \tag{8}$$

$$\delta = d/R_c \tag{9}$$

where R_c is the radius of curvature.

Figure 10 depicts the relation between curvature and Reynolds number. The red circles in Figure 10 illustrate Dean numbers of 242 at $Re = 500$ and $h/d = 1.0$ and of 237 at $Re = 375$ and $h/d = 2.0$. Similarly, the blue circles in Figure 10 show Dean numbers of 181 at $Re = 375$ and $h/d = 1.0$ and of 237 at $Re = 250$ and $h/d = 4.0$. The vortex structures in both cases show

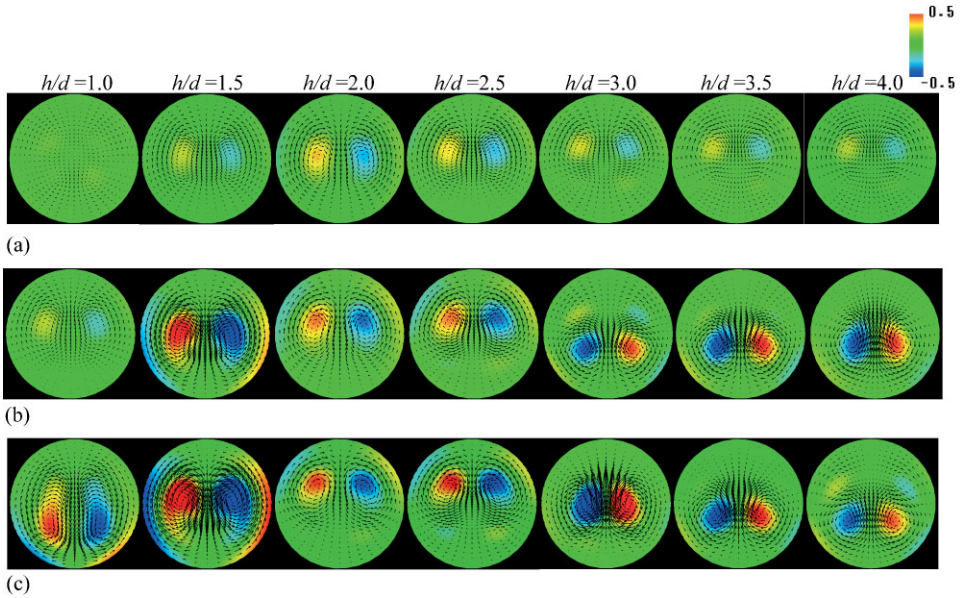

Figure 8. Vortex structures of secondary flow in the section D with respect to curvature h/d and Reynolds Number Re: (a) $Re = 250$; (b) $Re = 350$; and (c) $Re = 500$.

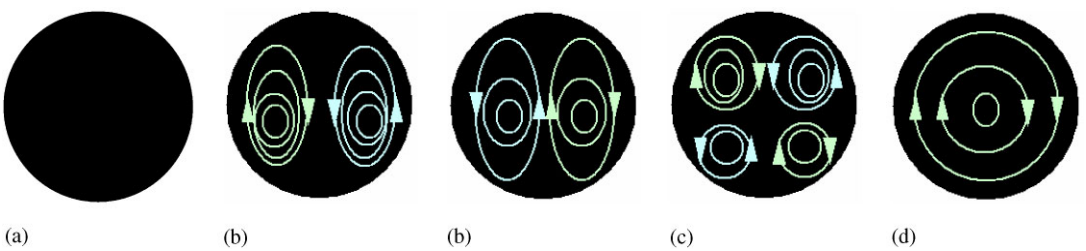

Figure 9. Classification of vortex structure of secondary flow for inflow model: (a) no vortex; (b) one pair of outward vortices and one pair of inward vortices; (c) two pairs of vortices; and (d) one vortex.

similar vortex structures (as shown in Figures 11(a.1)–(b.2)). Thus, the vortex structures can be categorized with respect to Dean number.

4.5. Vortex structures of secondary flow at pulsatile inflow boundary conditions

Because blood flow is pulsatile, simulations at pulsatile inflow boundary conditions were conducted for the curved pipe model. Inflow boundary conditions are prescribed by the velocity measured by ultrasound Doppler as shown in Figure 12(a). The Reynolds number varies from 80 to 480 over one cardiac cycle.

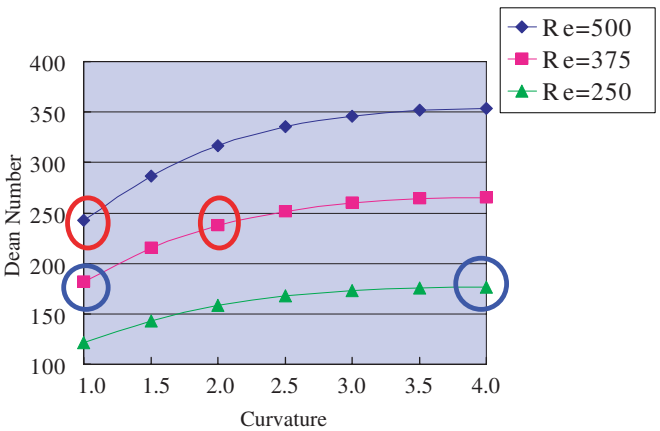

Figure 10. The Dean number with respect to curvature and Reynolds number.

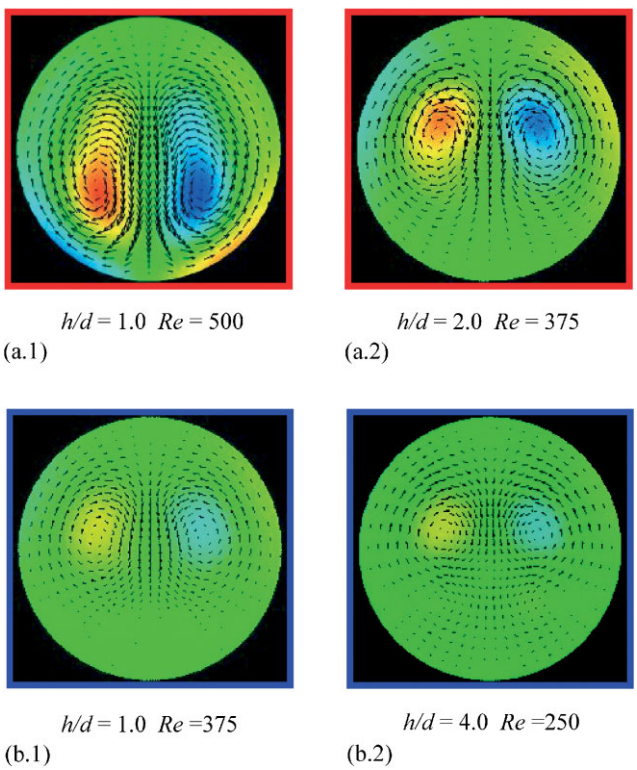

Figure 11. The vortex structures of secondary flow in terms of Dean number: (a.1) $N_D = 242$; (a.2) $N_D = 237$; (b.1) $N_D = 181$; and (b.2) $N_D = 176$.

Figures 12(b.1)–(b.6) show the evolution of vortex structures of secondary flow in section D at curvature $h/d = 3.5$ over one cardiac circle. Figures 12(b.1)–(b.3) describe the vortex structure during systole (0.0–0.08 s), while Figures 12(b.4) and (b.5) show

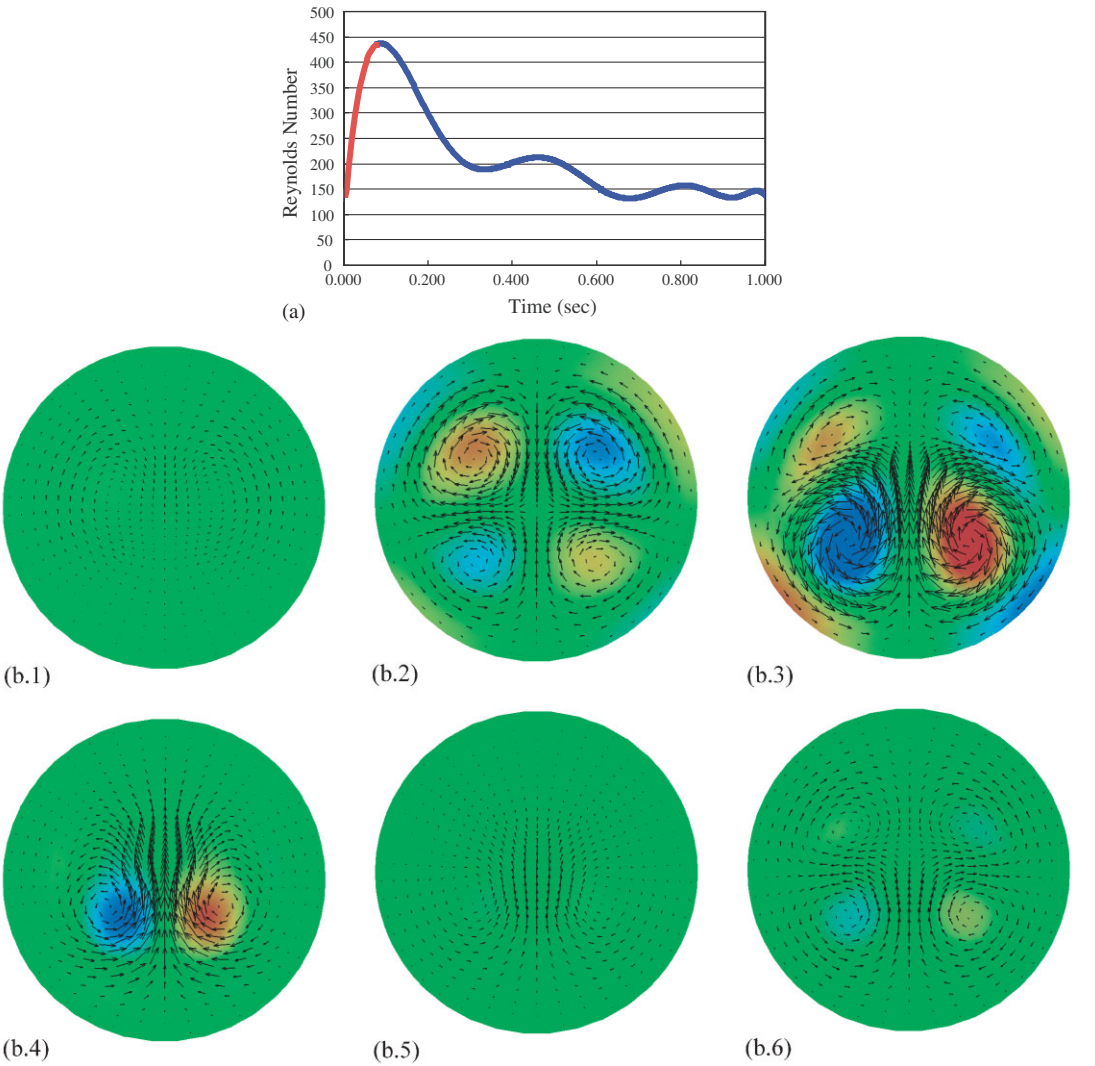

Figure 12. Evolution of vortex structures of secondary flow in section over one cardiac cycle: (a) inflow velocity in terms of the Reynolds number over one cardiac cycle; (b.1) 0.0 s; (b.2) 0.05 s; (b.3) 0.08 s; (b.4) 0.13 s; (b.5) 0.32 s; and (b.6) 0.45 s.

the vortex structure during diastole (0.08–1.0 s). The change in vortex structure is associated with Reynolds number as seen in the simulations at the steady inflow boundary conditions. No vortex is present at 0.0 s. One pair of outward vortices appears at 0.025 s. The centreline of the vortex moves upward as the Reynolds number increases and a small pair of vortices appears in the bottom at 0.04 s. The lower pair of vortices grows and becomes two pairs at 0.08 s, the peak of systole. The upper pair decay and the bottom pair of inward vortices become dominant at 0.13 s. As the Reynolds number decreases, the vortices decrease at 0.3 s. However, two pairs

of vortices appear that are associated with an increase in Reynolds number at 0.4 s; the lower pair of vortices decay until disappearing and the pair of outward vortices become dominant at 0.5 s before decaying completely.

Based on these simulation results, the vortex structures of secondary flow were included in the model of the inflow boundary conditions. Because the axial components of the inflow velocities are provided by ultrasound Doppler measurements, the secondary components are superimposed on the Womersley velocity profile. The vortex structures are determined by curvature and Reynolds number, namely Dean number according to the classification shown in Figure 9. The magnitude of secondary flow is modelled to reproduce the evolution of the vortex structures.

5. IMAGE-BASED SIMULATION

5.1. Analysis model

The present model of the inflow boundary conditions is applied to the simulation of a MCA aneurysm, as shown in Figure 13. The model was constructed from CT images from a 68-year-old woman. Segmentation of the blood vessels was conducted using the threshold values and surface construction was obtained using the Marching Cubes method [3]. The diameter of the artery was 2.5 mm, and its length, including the aneurysm, was 30 mm. The number of modes was 62 080, and the number of elements was 56 526.

5.2. Numerical results

The simulations were performed for two different inflow boundary conditions: (1) an inflow model without secondary flow, and (2) an inflow model with secondary flow. The inflow

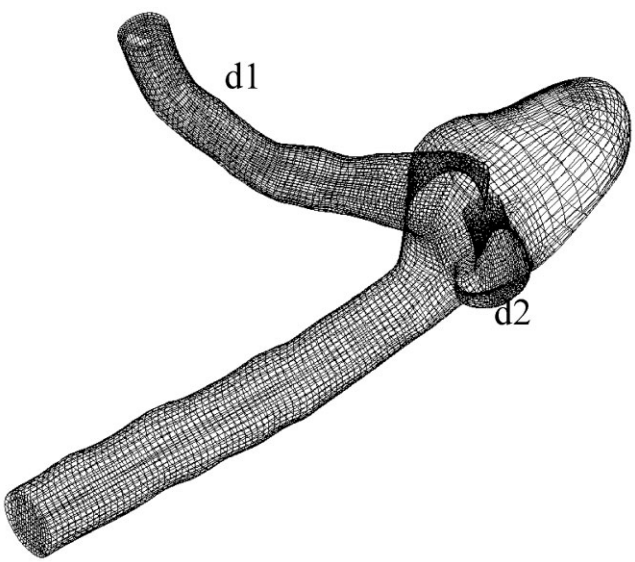

Figure 13. Analysis model of middle cerebral aneurysm.

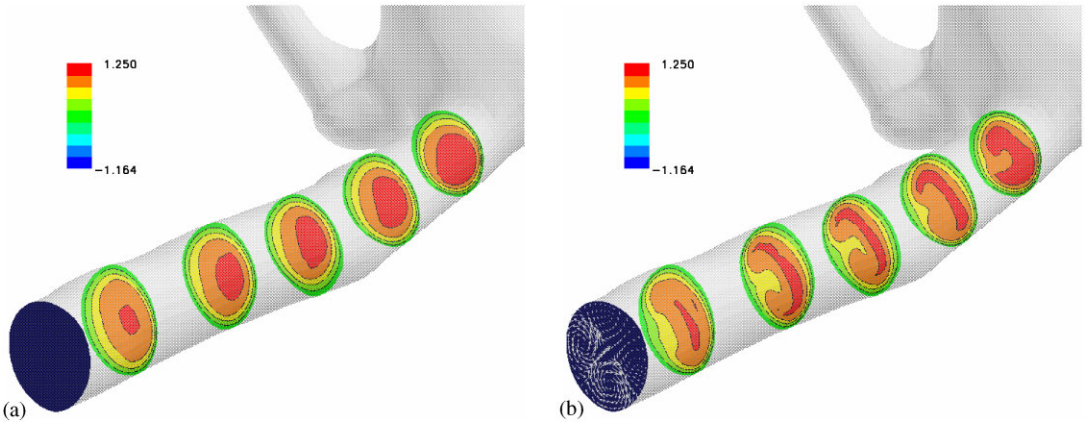

Figure 14. Comparison of streamwise velocity distribution in MCA at the peak of systole between inflow models without and with secondary flow: (a) inflow model without secondary flow; and (b) inflow model with secondary flow.

was based on numerical results from the curved pipe model for pulsatile inflow conditions. The secondary flow components were superimposed on the Womersley profiles, depending on curvature and Reynolds number.

Figures 14(a) and (b) compare the streamwise velocity distributions in the MCA at the peak of systole, $t = 0.08$ s, between the inflow models with and without secondary flow. Because the Reynolds number reaches its greatest value at $t = 0.08$ s, the vortex structure become two pairs of vortices, as shown in Figure 14(b). The streamwise component of flow tends to shift toward the wall of bifurcating artery d2 due to secondary flow. Thus, blood flow into the aneurysm is distributed uniformly in the model without secondary flow, while blood flow tends to concentrate on the bottom of the aneurysm in the model with secondary flow, as shown in Figures 15(a) and (b).

Wall shear stress exerts a strong influence on various functions of endothelial cells [10]. Figures 16(a) and (b) show the difference in wall shear stress distributions from 0.06 to 0.08 s during systole for inflow models with and without secondary flow. In particular, the inflow model without secondary flow indicates that wall shear stress tends to concentrate in one area. In contrast, the model with secondary flow does not contain a peak, and overall wall shear stresses are smaller than those in the model without secondary flow.

Thus, the results of the simulations demonstrate that secondary flow affects the velocity and wall shear stress fields. Medical velocity measurements obtained by MRI or ultrasound Doppler provide only axial velocity. However, other velocity components in the inflow boundary flow are important for evaluation of some conditions.

6. CONCLUSIONS

Boundary conditions play an important role in image-based simulations. This study investigated inflow boundary conditions to determine the effects of secondary flow on haemody-

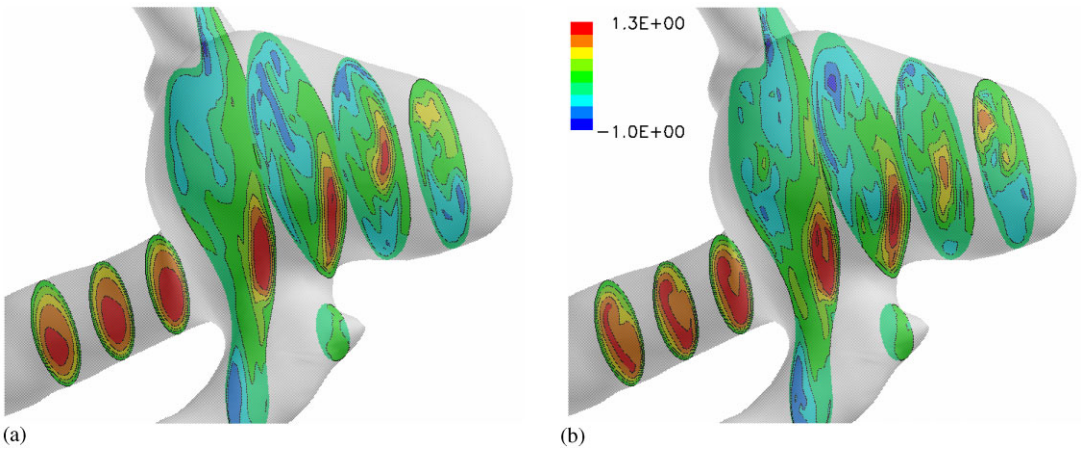

Figure 15. Comparison of streamwise velocity distribution in the aneurysm at the peak of systole between inflow models without and with secondary flow: (a) inflow model without secondary flow; and (b) inflow model with secondary flow.

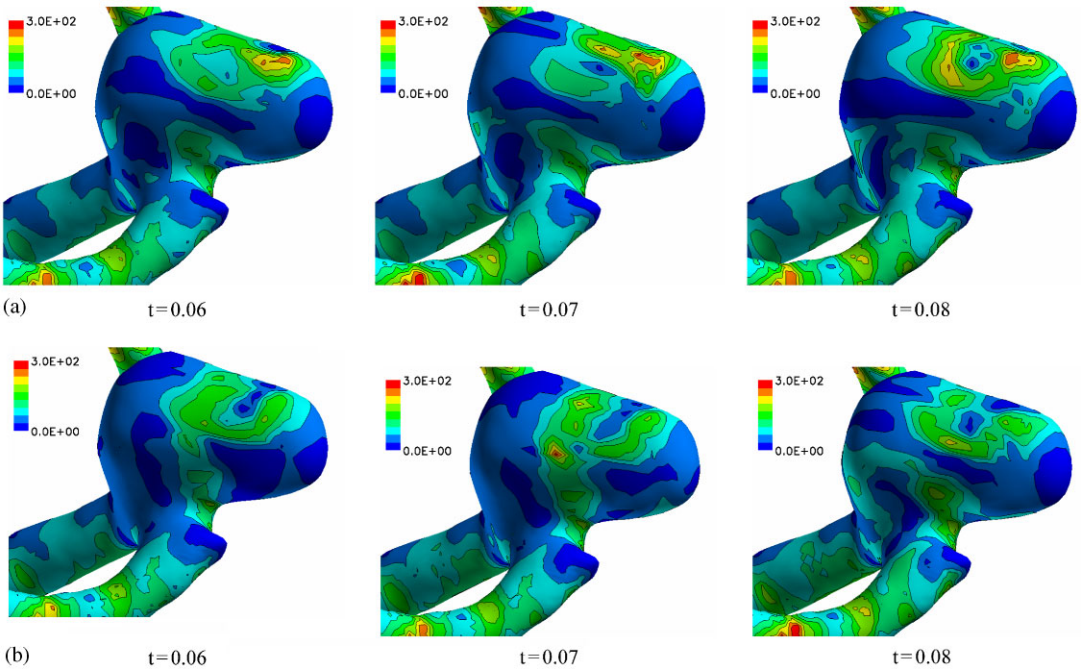

Figure 16. Comparison of wall shear stress distribution in the aneurysm at the peak of systole between inflow models without and with secondary flow: (a) inflow model without secondary flow; and (b) inflow model with secondary flow.

namics. First, simulations were conducted using the curved pipe model, which emulates the curvature of ICA, and the results were compared with PIV measurements. The numerical results of the simulation correlate well with PIV measurement data. Second, simulations were conducted using the curved pipe model to examine the vortex structures of secondary flow by varying curvature and the Reynolds number under steady state and pulsatile flow conditions. The resulting vortex structures of the secondary flow on the outflow condition from the simulations are modelled based on the Dean number, which is a function of curvature and Reynolds number. Third, the modelled secondary flow as a function of Dean number was combined with velocity measurement data obtained by ultrasound Doppler and used as the inflow boundary conditions for the image-based simulation. Comparison of the simulation results from inflow models with and without secondary flow showed differences in velocity and wall shear distributions between the two models. Thus, the influence of secondary flow on inflow boundary conditions is not negligible and should to be considered.

REFERENCES

1. Taylor CA, Draney MT, Ku JP, Parker D, Steele BN, Wang K, Zarins CK. Predictive medicine: computational techniques in therapeutic decision-making. *Computer Aided Surgery* 1999; **4**:231–247.
2. Cerbral JR, Yim PJ, Lohner R, Soto O, Choyke PL. Blood flow modeling in carotid arteries using computational fluid dynamics and magnetic resonance imaging. *Academic Radiology*.
3. Oshima M, Takagi K, Hyakawa M, Torii R, Nagano K. Effects of vascular morphological changes on cerebral haemodynamics. *Journal of Biomechanics*, submitted.
4. Oshima M, Torii R, Kobayashi T, Taniguchi N, Takagi K. Finite element simulation of blood flow in the cerebral artery. *Computer Methods in Applied Mechanics and Engineering* 2001; **191**:661–671.
5. Olfsen MS, Peskin CS, Kim WY, Pedersen EM, Nadim A, Larsen J. Numerical simulation and experimental validation of blood flow in arteries with structured-tree outflow conditions. *Journal of Biomechanics* 2000; **28**:1281–1299.
6. Wan J, Steele B, Spicer S, Strohband S, Feijoo GR, Hughes TJR, Taylory CA. A one-dimensional finite element method for simulation-based medical planning for cardiovascular disease. *Computer Methods in Biomechanics and Biomedical Engineering* 2002; **5**:195–206.
7. Cassot F, Zagzoule M, Marc-Vergnes J-P. Hemodynamic role of the circle Willis in steonoses of internal carotid arteries: an analytical solution of a liner model. *Journal of Biomechanics* 2000; **33**:395–405.
8. Torii R, Oshima M, Kobayashi T, Takagi K. Numerical simulation system for blood flow in the cerebral artery using CT imaging data. *JSME International C* 2001; **44**:982–989.
9. Raffel M, Willert C, Kompenhans J. '*Particle Image Velocimetry*'—*A Practical Guide*. Springer: Berlin, 1998.
10. Malek AM, Apler SL, Izumo S. Hemodynamic shear stress and its role in atherosclerosis. *Journal of the American Medical Association* 1999; **282**:2035–2042.

